Mesoscale Machine Learning Analytics for Electrode Property Estimation

Venkatesh Kabra,[1] Brennan Birn,[1] Ishita Kamboj,[2] Veronica Augustyn,[2] and Partha P. Mukherjee[1,z]

[1]School of Mechanical Engineering, Purdue University, West Lafayette, Indiana 47907, United States

[2]Department of Materials Science and Engineering, North Carolina State University, Raleigh, North Carolina 27695, United States

[z]*Correspondence:* pmukherjee@purdue.edu (P. P. Mukherjee)

Abstract:

The development of next-generation batteries with high areal and volumetric energy density requires the use of high active material mass loading electrodes. This typically reduces the power density, but the push for rapid charging has propelled innovation in microstructure design for improved transport and electrochemical conversion efficiency. This requires accurate effective electrode property estimation, such as tortuosity, electronic conductivity, and interfacial area. Obtaining this information solely from experiments and 3D mesoscale simulations is time-consuming while empirical relations are limited to simplified microstructure geometry. In this work, we propose an alternate route for rapid characterization of electrode microstructural effective properties using machine learning (ML). Using the Li-ion battery graphite anode electrode as an exemplar system, we generate a comprehensive dataset of ~17000 electrode microstructures. These consist of various shapes, sizes, orientations, and chemical compositions, and characterize their effective properties using 3D mesoscale simulations. A low dimensional representation of each microstructure is achieved by calculating a set of comprehensive physical descriptors and eliminating redundant features. The mesoscale ML analytics based on porous electrode microstructural characteristics achieves prediction accuracy of more than 90% for effective property estimation.

Keywords: data-driven models, machine learning, electrodes, mesoscale modeling

Introduction:

Li-ion batteries (LIBs) have advanced from powering mobile electronics to revolutionizing ground transportation, and are now considered for electric urban air mobility[1–4]. LIBs are highly efficient energy storage systems used in conjunction with renewable energy generators, contributing to a greener future. The interest in battery material research and the advancement in characterization techniques has led to an exponential amount of data available for finding optimal battery candidates. The use of data-driven methods such as machine learning (ML) can enable the screening through a large material, composition, and microstructural space, enabling rapid innovation[5–12].

Developing a structure-property relationship is critical because it can guide the improvement of electrochemical performance through the composition, and morphological control of the mesostructure. The state-of-the-art LIB electrode consists of active material (AM), and conductive additive binder domain (CBD) assembled into a composite porous mesostructure. The AM exhibits a larger characteristic length scale compared to the CBD and together they form a solid structural matrix with multi-length scale features[13–16]. For proper functioning of an electrode, it requires these multiple components including AM and CBD, because an electrode performs a complex range of processes while the battery operates. The role of AM particles is to store the chemical energy in form of Li and to provide a high reaction surface area for electrochemical redox reactions during the battery operation. The electrochemical reaction generates Li^+ ions and electrons, the solvated ions shuttle through the tortuous pores of the electrode towards the opposite electrode where it reduces and intercalates into it. The CBD phase aids in improving the mechanical connection and electronic percolation pathways through the electrode for their travel towards the current collector[17–19]. The electrode mesostructure enabling these three critical physical processes can have a varying chemical composition (AM, CBD porosity), active material particles with different shapes, sizes, orientation, and CBD morphology[20–23]. Ongoing research effort aims to improve electrochemical performance at these hierarchies of length scales[24–27] and mesostructure tuning has been used such as for ion transport improvement by forming aligned pores in the electrode[28–31], bi-tortuous electrode structures[32,33], and CBD morphology tuning[13].

To comprehend the reaction and transport dynamics, the electrode is characterized using effective microstructural property based on effective medium approximations[34]. It provides a convenient macroscale description of the microscale physical processes within an electrode. The conventional approach to this problem of determining effective electrode properties is to perform experiments measuring the effective properties using experimental techniques, including electrochemical impedance spectroscopy, galvanostatic intermittent titration, and Brunauer–Emmett–Teller (BET) methods for interfacial area[35–41]. The issue with experimental characterization is the significant cost, time, and effort. Repeating this for a very large number of constructions of electrode structure with varying microstructure topology is also a challenge. This can be overcome by the usage of physics-derived models which replicate the electrode's physical mechanisms. The characterization of electrodes using direct numerical simulation on X-ray tomography images and focused ion beam/scanning electron microscopy (FIB-SEM) images is another approach[42–45]. The limited availability of tomography imaging data can be overcome by the use of stochastically generated electrode mesostructures. This can be generated methodically by specifying the composition (volume fraction of active material, carbon-binder phases), particle size distribution, and orientation of particles. Consideration of each parameter grows the design space exponentially leading to a comprehensive dataset with ~17000 mesostructures along with freedom for generating unique microstructures currently beyond the reach of common electrode fabrication methods. The stochastic algorithm for generation involves filling a domain with a specified particle geometry and alignment till it reaches the target volume fraction. Once a backbone electrode structure with the active material particle is generated, the carbon-binder phase is added to the structure[13,43,46]. This is a highly scalable method for generating specified composite electrode structures, which can be characterized for kinetic and transport effective properties.

Developing a structure-property relationship is a perfectly suited problem to take advantage of machine learning (ML) methods and applications. ML methods are a class of algorithms that self-learn the complex relations in high-dimensional datasets. Supervised ML methods, trained over comprehensive known datasets, can learn the dependence of input conditions over the output values and provide physical insights into high dimensional data without the need for prespecified physical governing laws[47,48]. These methods can also reveal physically fundamental relations and make quantitative and qualitative predictions for unknown scenarios. For the electrode effective properties, this can be used towards its advantage to study the intricate relationship between electrode structure and properties. ML methods are used in battery research to understand issues such as degradation and safety. They were used to predict the state of charge and state of health of a battery using electro-impedance spectroscopy[49,50], internal short circuit detection[49], optimal safety under abuse testing[51,52], capacity fade, and remaining useful life predictions[53–57] and effective porous media properties[58–61].

Problem Description:

In this work, we develop a mesostructure–effective property framework for a graphite-based electrode as an exemplar system. As a first step, we stochastically generate comprehensive electrode structures ranging in density and with various binder topologies. By using pore-scale simulations we characterize the electronic conductivity, tortuosity in three directions, and various interfacial areas. The electrode structure is quantitatively described by characteristics such as the composition, particle shape, and pore size which serve as inputs with effective properties as the outputs of the dataset. The physical descriptors are selected to diversify the patterns in the input datasets, and data cleaning methods are used to remove redundant features and outliers within the data. We trained and tested various supervised machine learning-based regression models and compared their accuracy in predicting effective properties.

Methodology:

The basic goal is to represent the effective property of the electrode structure as a function of the electrode's physical descriptor using ML as a tool. On one hand, the effective properties such as tortuosity, electronic conductivity, and specific surface area are a representation of the electrode's macroscale reactive-transport behavior. To capture the structural differences between electrode microstructure, it is also represented by the physical descriptors in a low dimensional space. These physical descriptors quantitatively represent electrode structure's morphology and for comprehensive characterization of the microstructure we propose four classes of the physical descriptor to quantify, including composition, active material shape, orientation, and pore phase.

Electrode structure generation

We used stochastic electrode generation in GeoDICT[62] to generate a realistic mesostructure consisting of an active material particle-based backbone. The 3-dimensionally generated active material skeleton has a cubical domain, with a volume of $200\times200\times200$ μm^3 as shown in Fig. 1(a). The Representative Volume Element (RVE) analysis was performed to ensure that the domain was representative of the electrode volume (refer to Supporting Information). Fig. 1(a) outlines the steps for the generation of realistic electrode mesostructures, and the range of compositions, particle sizes, and orientations used in this study. Since imaging experiments show that graphite active material particles form microscale ellipsoidal structures[63], the active material particle shape was set as an ellipsoid. In some cases the graphite particle shape can deviate due to irregular, flaky, or fibrous particle geometry, and the particle size might also follow a distribution but it is not considered here. The ratio of the length of the ellipsoid's major to minor axes varied between 0.5 to 5, with ratio 1 being a special case for spherical particles. The AM volume fraction varied from 40 to 80 %, ranging from a sparsely to densely packed electrode structure. The particle orientation was varied using anisotropy parameter values between 0.1 to 100. Finally, 5 to 10 vol.% of binder was added to the generated active material backbone using an interfacial energy-based stochastic deposition. The morphology factor (ω) is a measure of cohesive to adhesive tendencies of binder over AM[13] which varied between 0.1 to 0.9. Smaller ω gives rise to a film-like deposit while higher ω gives rise to a finger-like deposit, generating various binder topologies with differing electron and ion transport pathways. Overall a comprehensive set of ~17000 unique realistic composite electrode structures was generated.

Outputs - Effective properties characterization:

To characterize the efficacy of the electrode architecture, we determine their effective properties by utilizing 3D-physics-based pore-scale simulations performed on the generated electrode structures (as shown in Fig. 1(b)): (1) $\sigma_e -$the effective electronic conductivity in three directions (which determines electron percolation), (2) $\tau -$tortuosity of pore network in three directions (Li^+ transport in the pore network). The calculation of the effective conductivity and tortuosity is based upon assigning suitable diffusivity (or conductivity) values to the pores and solid phases and performing a concentration (or charge) balance. Concentration (or electric potential) Dirichlet boundary conditions are applied at the two opposite faces and the effective properties are calculated in the three orthogonal directions (X, Y, and Z) as shown in Fig. 1(b). The last effective property under consideration is (3) a_s – volume-specific surface area (interfacial area available for the electrochemical reaction). In a composite electrode, there are three two-phase interfaces: the pore-active material interface (a_{01}), the pore-binder interface (a_{02}), and the active material-binder interface (a_{12}). The electrochemical redox reaction occurs over the pore-active material interface a_{01}, while the other two interfaces a_{12}, and a_{02} are electrochemically inactive[13].

Inputs - Electrode Physical Descriptor Characterization:

Composition: It is the lowest order representation of electrode microstructure information similar to a zero-order moment, quantifying the volume and weight fraction of the chemical constituents present in the composite electrode matrix. For a model intercalating electrode, like graphite consisting of three distinct phases: active material, binder, and pore phase, the unique composition of the electrode is determined from the volume fraction of active material (v_{AM}), the volume fraction of the secondary phase (v_S), and secondary phase morphology parameter (ω); Fig. 1(c)). Since pores, active material, and secondary phases add up to 100 vol.%, the porosity is uniquely determined by the other composition.

Another unique parameter we proposed as part of this *composition* description is the overlap factor (γ) which quantifies the overlap between the intersecting particles. It is quantified as the fraction of overlapping volume to the actual volume occupied by the active material particles as shown in Fig. 1(c) and quantified in Eq. (1). From the schematic in Fig. 1(c), we define V_1, V_3 refers to non-intersecting volume while V_2 is the shared volume. From a low energy density electrode structure to a high energy density electrode the overlap of AM particles is expected to increase and so is the overlap factor. It can be readily observed from Fig. 2(a) that the overlap-factor increases when the radius of the active material particle increases and porosity decreases. The highest overlap factor of ~0.79 is seen when large particles are packed in a low porosity configuration, while it takes the lowest value of 0.2 when smaller particles are packed in a high porosity configuration.

$$Overlap-factor\,(\gamma)=\frac{V_2}{V_1+V_2+V_3} \tag{1}$$

Active material shape: It is the deeper level information of about the particle structure and it determines the morphology of the electrode structure and pore space. In this work, we have considered a variety of particle geometries of the AM particles which deviate significantly from a well-rounded spherical shape. So to generalize we redefined the active material particle geometry into well-known shape descriptors:

Equivalent radius: The equivalent radius for an AM particle is the radius of a sphere enclosing an equal amount of volume as the particle. The formula for it is described in Eq. (2), where V refers to the single-particle volume. Fig. 1(c) schematically describes the equivalent radius concept for an ellipsoid particle. A regular ellipsoid’s shape can be modified by varying the ratio of its axes' length. Increasing any single-axis length will lead to angular and pointed particles while increasing the two-axis length will create an oblate-shaped particle. Fig. 2(b) shows that as the particles become more angular/oblate their equivalent radius increases proportionately, ranging between 2 to 7 µm.

$$R_{eq}=\left(\frac{3V}{4\pi}\right)^{\frac{1}{3}} \tag{2}$$

Eccentricity: It measures the elongation of the particle, defined as the ratio of the longest chord of the particle to the shortest chord (Eq. (3)). The schematic in Fig. 1(c) shows that for an ellipsoid particle, this translates to the ratio of the major axis to minor axis length. Eccentricity (e) measures the elongation of the particle along a particular direction (Eq. (3)), with 'a' being the longest axis and 'c' being the shortest axis length. When only the largest ('a') axis length is increased in an ellipsoid particle, it leads to the formation of angular particles (Fig. 2(c)) as seen with the increase in eccentricity.

$$Eccentricity(e) = \frac{\text{longest axis}}{\text{shortest axis}} = \frac{a}{c} \tag{3}$$

Rectangularity: Rectangularity is defined as the ratio of the surface area of a particle to the surface area of the minimum bounding rectangle surrounding it in 3D (a cuboid; Eq. (4)), and schematically described in Fig. 1(c). In Eq.(4), S_{AM} refers to the area of active material particle and S_{cuboid} refers to the area of the cuboid surrounding it in 3-dimensions. When the aspect ratio of the active material is changed, its rectangularity varies from 0.53 to 0.61 as shown in Fig. 2(d). It shows that spherical particles have the smallest rectangularity while more oblate or angular particles have higher rectangularity.

$$\text{Rectangularity } (\rho) = \frac{\mathrm{S}_{AM}}{\mathrm{S}_{\text{cuboid}}} \tag{4}$$

Sphericity: The sphericity (ψ) of an ellipsoid particle is used to quantify the closeness of a particle in resembling a sphere. In Eq. (5), 'V' refers to the volume of active material and S refers to its surface area. It is known that a sphere has a minimal surface area for enclosing a given volume, hence sphericity is always less than or equal to one; a smaller value denotes divergence from spherical characteristics (Fig. 1(c)). Fig. 2(e) denotes the sphericity of the particle under consideration, it is maximum with the value of 1.0 when they are perfectly spherical on the other hand the oblate ellipsoid particles are the least spherical with a sphericity of 0.65.

$$Sphericity\,(\psi) = \left(\frac{\pi^{\frac{1}{3}} (6V)^{\frac{2}{3}}}{S} \right) \tag{5}$$

Pore phase: Quantification of the pore phase is critical since it controls the transport dynamics of Li^+ ions within the electrode. Since porosity is a low-level representation of the porous microstructure, here we resort to pore size to quantify the efficacy of porous percolation pathways. We have used the 3D-continuous pore size distribution (c-PSD) definition by Munch and Holzer[64] using the open-source implementation in Fiji[65]. In this method we calculated the closest distance of the active material interface from each pore voxel, resulting in a distance map function. From this function, the volume fraction of the pore phase which can contain a sphere with a certain radius is calculated. Fig. 1(c) schematically describes the pore size distribution for a sample electrode microstructure where differently sized pores are fitted within the pore space of the microstructure. This results in a pore size distribution (PSD) with the radius of the pore phase plotted against the volume fraction of the pore phase covered (refer to supporting information for details). Fig. 2(f) shows the mean pore size (φ) of the microstructure with the radius of AM particle and its porosity. The highest mean pore size of about 7μm is seen when large particles are packed in a high porosity configuration meanwhile when smaller particles are packed with low porosity configurations, they have the smallest pore sizes.

Orientation: The electrode microstructure needs to be quantified for its anisotropic characteristics and quantify the degree of alignment of active material particles. Since we know the physical effective properties (e.g. conductivity and tortuosity) of the electrode are a strong function of the particle network because these particles form the basis for the electron percolation pathways, and subsequently, also determine the complementary pore network. When stochastically generating the electrode microstructure, a random direction is computed (x, y, z), then the particle alignment is determined using anisotropy parameters 1 and 2 (a_1, a_2) which denote the strength of orientation of active material particles. The direction of each AM particle is set based on direction vector (d_a) which is a function of the Anisotropy parameter as shown in Eq. (6).

$$d_a = \begin{pmatrix} x_a \\ y_a \\ z_a \end{pmatrix} = \frac{1}{\sqrt{(a_1 x)^2 + (a_1 a_2 y)^2 + z^2}} \begin{pmatrix} a_1 x \\ a_1 a_2 y \\ z \end{pmatrix} \tag{6}$$

Thus, for different generated electrode mesostructures, we have varied the alignment by changing the values of anisotropy parameters (a_1, a_2) between 0.1 to 100, generating structures with anisotropic orientation in different directions as well as some with isotropic characteristics as schematically shown in Fig. 1(c).

Results and Discussion:

Correlation of effective properties with descriptors:

We investigate the correlation of each effective property (tortuosity, electronic conductivity, and interfacial area) with the electrode's physical descriptors i.e. Composition, Active material shape, Pore phase, and Orientation. To analyze the trends within the comprehensive dataset of electrode microstructure under consideration, we segregate them into two categories to study the impact of the orientation of the particle and the morphology of the particle.

The direction of arrangement of these particles becomes critical when particles are not symmetric i.e., for non-spherical morphologies. The arrangement in a particular direction for these asymmetric particle morphologies gives rise to an anisotropic electrode microstructure with direction-dependent properties. The figures Fig. 3, Fig. 5, and Fig. 7 are for a fixed ellipsoid morphology of the particles, which can be aligned in the transport direction (Z-direction), randomly aligned, or aligned perpendicular to the transport direction respectively.

The second set of figures is based on a shape classification scheme established by the Zingg diagram[66], where ellipsoid particles are segregated into various regimes based on the relative axes lengths of the ellipsoid as shown in Fig. 4(a). To have a comprehensive dataset of AM particle shape i.e. to consider all types of shape (ellipsoidal) effect, during the electrode structure generation particle axis lengths have been carefully chosen to include all classes. This leads to having various geometrical shapes representative of all the different classes of ellipsoids and leads to generalizable ML models not limited to a particular particle geometry. All the particle shapes within the current dataset have been marked with colored dots, and are mapped onto the classification scheme in Fig. 4(a). We see that the triaxial ellipsoid particle shapes can take the form of bladed, prolate, oblate, and spherical shapes. While the spherical shape is obvious, the bladed particles have all three different axis lengths, oblate particles are shaped like flattened spheroids like M&M while prolate particles are elongated spheroids like a rugby ball[63] (For details refer to Supporting Information). The shape effects have been studied in Fig. 4, Fig. 6, and Fig. 8.

Tortuosity:

Traditionally in the modeling of LIB, the porous electrode microstructure is assumed to be consisting of non-overlapping spherical active material particles with two phases including AM and pores. Based upon this idealistic representation the empirical Bruggeman's law predicts the tortuosity of an electrode's pore space as a function of only the porosity of structure as shown in Eq. (7), and shows the scaling as the inverse of the square root of porosity. Various extensions of

Bruggeman's law have been made to express tortuosity as different power from the porosity of structure. As such, there is no generalized analytical relation for predicting tortuosity as a function of the microstructural parameters, except in specialized cases such as simple isotropic and non-overlapping highly porous structures without the presence of additional phases[67–69].

$$\tau = \varepsilon^{-0.5} \tag{7}$$

Fig. 3 investigates the pore space tortuosity of the electrode microstructure with the varying alignment of ellipsoidal particles. Fig. 3(a)-(c) are for a fixed ellipsoid morphology of the particles, which can be aligned in the transport direction (Z-direction), randomly aligned, or aligned perpendicular to the transport direction respectively. Across all these scenarios we observe that the tortuosity increases as the porosity of the structure decrease due to the pore size constriction at higher packing. The different colors represent the range of tortuosity values at a given porosity since factors such as particle size and binder-phase morphology also play a role. We observe that the band of tortuosity values exhibited at a given porosity increases as the porosity decreases, this is because the sensitivity to the microstructural parameters increases at higher packing. Fig. 3(a) shows that the tortuosity of the structure in the Z-direction is smaller compared with that across X, and Y directions, due to the preferential alignment of particles in that direction. While Fig. 3(b) shows that, although these particles are spherically asymmetric when they are aligned randomly, they behave as isotropic structures with equal tortuosity in all directions. Finally from Fig. 3(c), we can compare across the X, Y, and Z-direction, we observe that there is a preferential direction of alignment of the particles perpendicular to the Z-direction, hence the Z-direction tortuosity is highest.

We plot Bruggeman's law for the three different exponents values: 0.5, 1, and 1.5, and observe the divergence from the power-law at high energy density and low-porosity electrode configurations because it does not consider the particle size, orientation. In Fig. 3(a) even for the high porosity configurations, we observe that the Bruggeman's coefficient is distinct in the three directions, with the X, and Y directions having a higher exponent than Z-direction due to the alignment in Z-direction. Bruggeman's coefficient in Z-direction is about ~0.9 which is similar to the one found by other researchers[21] due to similarity in ellipsoidal shape characteristics and alignment in the transport direction. Fig. 3(b) shows that Bruggeman's coefficient is identical in all three directions due to the isotropic nature of the structure, with a coefficient value of ~1.2, which is higher than for the aligned structure in Fig. 3(a). For Fig. 3(c) where the alignment is perpendicular to Z-direction, the coefficient in Z-direction is higher compared to the other two directions, with a value of ~1.25 while for Y-direction ~0.9.

Fig. 4 investigates the impact of active material particle shape over the effective electrode properties with the random alignment of particles. All the particle shapes within the current dataset have been marked with colored dots, and are mapped onto the classification scheme in Fig. 4(a), and discussed above. Fig. 4(b) shows that across the various shape characteristics, if the randomly aligned particle is the choice, the minimum tortuosity is exhibited by the microstructure consisting of spherical particles for higher porosities ($\varepsilon \geq 0.3$). While the next best choice is to consider the prolate particles, followed by bladed and oblate particles. A potential reason for this ordering is that since these are randomly oriented particles when encountering the spherical particle, they provide an idealized smallest smooth pathway from one point on the surface to the other diametrically opposite end irrespective of the orientation. On other hand compare with the oblate particles, which are an idealized version of platelet morphology found in the graphite[63], the shortest path connecting the two faces of the ellipsoid requires traversing along the longest major axis as shown in Fig. 4(b). Within Fig. 4(b) we also observe that Bruggeman's law which is limited to higher porosities, Bruggeman's coefficients are different across various shapes, with oblate particles having the highest coefficient followed by the bladed, prolate, and spherical particles. This coefficients order is in good agreement with the existing literature and verifies the validity of the simulations and structures[21]. At lower porosities ($\varepsilon \leq 0.3$), generalizing the order of tortuosity values for different particle shapes becomes more difficult as can be seen in Fig. 4(b) except that spherical particle still provides the lowest tortuosity. At these lower porosity, the range of tortuosity values spanned by each particle shape is quite high. This is discussed earlier and follows from the fact that tortuosity becomes more sensitive to particle arrangement and characteristics at lower porosities and even the slightest of changes to particle arrangement can cut off the percolation pathway resulting in highly tortuous structures. We can also justify this based on Fig. 4(c), which shows that the tortuosity is a function of the mean pore size of the microstructure. For the larger pore sizes ($\geq 4.5\mu m$), oblate particles offer the highest tortuosity compared to all, implying that they distort the pore space significantly more compared to the other particle shapes. As the mean pore size becomes smaller ($\leq 4.5\mu m$) or equivalently lower porosity structures the tortuosity order becomes more complicated with all the particle morphologies having similar tortuosity values.

Electronic Conductivity:

The electronic conductivity of a microstructure measures its efficacy at transporting electrons with minimal losses, within these structures only active material particles participate while binder (polyvinylidene fluoride) and pores have no contribution because of very low intrinsic electronic conductivity. Here the electronic conductivity is normalized by the intrinsic electronic conductivity of the AM particle to limit the variation between 0 to 1. Fig. 5(a)-(c) investigates electronic conductivity for a fixed ellipsoid morphology of the particles, which can be aligned in the transport direction (Z-direction), randomly aligned, or aligned perpendicular to the transport direction respectively. Across all these scenarios we observe that the electronic conductivity increases as the porosity of the structure decrease due to the increasing overlap and creation of numerous wide electronic pathways across the structure as seen in Fig. 6(a). The different colors represent the range of electronic conductivity values at a given porosity since factors such as particle size and binder-phase morphology also play a role. From Fig. 5(a) we observe that the electronic conductivity in Z-direction is about ~20-30% higher compared to the X and Y direction, due to the alignment of the particles parallel to the transport direction, resulting in higher overlap/electronic pathways. Fig. 5(b) on other hand shows the electronic conductivity for the same type of ellipsoidal particle except with random alignment. Here the electronic conductivity shows equal values in all directions due to the isotropic behavior of randomly oriented particles. Fig. 5(c) represents the scenario with particle alignment perpendicular to the transport direction, due to which Z-direction conductivity is quite smaller compared to the X, Y direction electronic conductivity. Across all cases from Fig. 5(a)-(c) we also observe that the anisotropicity of electronic conductivity decreases for lower active material v.f. (v_{AM} <0.5), probably because of insignificant overlap of the particles, hindering any directional preference.

Fig. 6 investigates the impact of active material particle shape over the effective electrode properties with the random alignment of particles. From Fig. 6(a) we observe the increase in the overlap of electrode AM particles which in turn increases electronic conductivity from ~0.1 to ~0.6 for the various shapes of the ellipsoids. Fig. 6(b) shows that at a higher volume fraction (v_{AM} ≥0.6), the electronic conductivity of particles with different shapes follows the order of sphere < prolate < bladed < oblate. Among these, spherical particles show minimal electronic conductivity, because the sphere has the minimum surface area for packing a given amount of active material volume. So, it is highly efficient at packing and minimizes contact with the other spherical particles causing fewer electronic conduction pathways. On the other hand, oblate particles due to their disk-like and angular characteristic provide shorter conduction pathways through their thickness as well as have significant overlap because of the high aspect ratio, improving electronic pathways. At a low volume fraction ($v_{AM} < 0.6$) there is no order in electronic conductivity, because of insufficient contacts and overlap, thus the slightest change can increase/decrease electronic conductivity increasing uncertainty. For all the differently shaped particles, increasing electronic conductivity tradeoffs with the increasing tortuosity of the structure as evident from Fig. 6(c). Although this tradeoff doesn't follow the linear trend, implying for a specific gain in electronic conductivity the corresponding tortuosity increases exponentially. The porous pathways are complementary to the particle network and thus more overlap of particles implies a more tortuous pathway for ion flow.

Interfacial Area:

One of the key critical properties of the electrode is the interfacial sites available at the active material interface for electrochemical reactions. The presence of three phases i.e. binder, active material, and pores lead to the formation of three interfaces pore-AM, pore-binder, and AM-binder, of which pore-AM is the electrochemically active interface[13]. Conventional modeling of LIB assumed the electrode microstructure to consist of perfectly spherical particles with no overlap, and with the presence of only two phases within the microstructure implying complete surface area is electrochemically active and available[19]. Based on this idealistic representation Bruggeman's empirical law predicts the specific surface area i.e. area per unit volume solely as a function of volume fraction and particle radius of AM as shown in Eq. (8). As such, there is no generalized analytical relation for predicting interfacial area except in the specialized case discussed above.

$$a_{01} = \frac{4\pi R^2}{\frac{4\pi R^3}{3v_{AM}}} = \frac{3v_{AM}}{R} \qquad (8)$$

Here we study the impact of various microstructural parameters including particle alignment (cf. Fig. 7) and shape (cf. Fig. 8), along with the comparison with the empirical law. Fig. 7(a) shows three different electrodes with identical characteristics including particle shape, morphology, and the v.f. of AM and binder phase. The distinguishing factor is the presence of particle alignment, leading to three cases either with Z-direction orientation, isotropic (random orientation), and oriented perpendicular to Z. There is minimal impact of particle alignment on the availability of surface area at the electrodes. This is because SSA is a scalar quantity, and the particle alignment does not change the particle overlap characteristics unlike the tortuosity and electronic conductivity values. Fig. 7(a) shows that empirical law is also applied to these microstructures for calculating the ideal SSA, but since the particles are not spherical, we use the equivalent radius of the ellipsoid particles as calculated using Eq. (2). We observe that for smaller AM volume fractions the actual specific surface area coincides with the empirical relation because the overlap of the particle is not significant. At higher A.M. volume fractions the actual specific surface area is less than the empirical predictions due to the overlapping of particles and binder phase covering interfaces as found in other work[13]. Fig. 7(b) shows the SSA as a function of normalized tortuosity for the three different particle alignments. The normalization is performed for the tortuosity of microstructure with randomly aligned particles. We observe that when particles are aligned in the transport direction, we can decrease the tortuosity by ~20%, with no trade-off to SSA, implying transport improvement in pores does not come at cost of sacrificing interfacial area. Fig. 7(c) shows the interfacial area as a function of normalized electronic conductivity (w.r.t. randomly oriented particles). We observe that the aligned particles not only improve the percolation pathways but also the electronic conduction pathways. The improvement in electronic conductivity is always higher than ~15% compared to the isotropic microstructures. For higher SSA the electronic conductivity improvements are even higher ~30%.

Fig. 8(a) represents SSA for various particle shapes as a function of their size/volume. The approximate SSA offered by the particles is ~10^6 m^2/m^3, showing that it increases exponentially as the volume of particles decreases. These values have been calculated for a single particle, to isolate the particle shape/size effect on microstructural characteristics. Among all shapes, for an identical volume, bladed particles offer the highest surface area, which is almost double that of a spherical particle which offers the least area. SSA does not follow a shape classification scheme, i.e. the oblate and prolate particles are quite dissimilar in their shape characteristics and even then they offer a similar specific surface area (cf. Fig. 8(a)). That is why no clear regime is established for the microstructure SSA based purely on particle shape itself in Fig. 8(b). Instead, we can see that microstructural characteristics such as AM volume fraction and the average dimension of the particle have a much more prominent impact and result in a non-monotonic trend. It is because at first, the pore-AM surface area increases when packing a higher AM fraction but beyond a certain v.f. it also causes more overlap of AM particles causing the surface area to reduce. This is also the reason we see the deviation of SSA from idealized values as shown by empirical relation. Fig. 8(c) shows the cumulative SSA of the pore-binder interface and it shows a similar non-monotonic trend due to increasing particle overlap.

In conclusion, the understanding of the microstructural complexations and their impact on the effective properties of the electrode can be utilized to improve the electrode design and electrochemical performance. Comparing the shape characteristics we observe that if the randomly aligned particle is the choice, the minimum tortuosity is exhibited by the microstructure consisting of spherical followed by the prolate, bladed, and oblate particles ($\varepsilon \geq 0.3$), while the electronic conductivity follows the opposite trend. The tradeoff between the electronic conductivity and tortuosity exists where AM packing linearly increases electronic conductivity while it leads to an exponential increase in tortuosity because the porous pathways are complementary to the electronic percolation pathways. The directional arrangement of particles is critical esp. for non-spherical morphology and gives rise to anisotropic electrode microstructure with direction-dependent properties including electronic conductivity and tortuosity. The alignment of particles can be used to minimize the tradeoff between tortuosity and electronic conductivity i.e. they can improve the porous percolation as well as electronic conduction pathways in the transport direction. Along with it the specific surface area i.e. electrochemically active area is not significantly affected by such particle alignment, although it is strongly affected by particle size and binder morphology.

Machine Learning-based workflow – Physical Descriptor-based Characterization:

Due to such a large number of microstructural descriptors and range of effective properties we need to determine a small yet representative descriptor set to predict these effective properties. Whereas the predictions based on the empirical laws such as Bruggeman's relation and specific surface area are valid only for high porosity and a limited range of electrode microstructure morphology.

The current machine learning workflow enables the solution to the key research question, i.e. describing the microstructural effective properties of the electrode in terms of its relevant physical descriptors. In principle, we achieve this through supervised machine learning methods applied to the microstructural dataset, with the effective property as output and physical descriptor as an input. We developed a 6-step strategy (c.f. Fig. 9):

Step 1: Generation of stochastic electrode microstructure with varying active material and secondary phase composition, the morphology of secondary phase, particle size, ellipsoid aspect ratio, and orientation of the particles. Characterizing these structures for effective properties including tortuosity, electronic conductivity, and interfacial area. (c.f. Fig. 1(b)).

Step 2: To accurately estimate the effective properties of the electrode microstructure, we have utilized a comprehensive dataset of physical descriptors capable of holistically characterizing a porous microstructure[70]. The rationale behind considering a variety of descriptors is that each of them quantifies the different aspects of the microstructure and collectively these descriptors exhaustively characterize the microstructure. These descriptors are defined such that it helps in reducing the biases introduced by only including handpicked descriptors specific to a microstructure type and instead it generalizes the machine learning procedure to be extensible to other porous microstructure systems. Here we have demonstrated this procedure for graphite as an exemplar system but it can easily be extended to other porous microstructure systems as well such as the nano-composites, solid-state cathode, thermal composites, etc. To describe the effective properties we have included a comprehensive electrode microstructure descriptor dataset including its: Chemical composition, Shape of active material, Pore phase constrictions, and Orientation of particles as shown in Fig. 9(a). The first category of the *composition* includes the volume fraction of various components including the active material phase (v_{AM}), conductive-binder phase (v_S), conductive-binder phase morphology, and overlap factor. These along with the overlap factor (γ) form the composition descriptors from D^1 to D^4 in Fig. 9(a). Since here we have considered various AM particle geometry, to generalize the model towards different shapes, we have comprehended them using equivalent radius (R_{eq}), Eccentricity (e), Rectangularity (ρ), and Sphericity (ψ). These descriptors fall into the category of *active material shape* descriptors set D^5 to D^8 as shown in Fig. 9(a). The third set of descriptors statistically quantifies the ease of porous ion percolation pathways, for which we resort to particle size distribution. From this distribution, we determine and use the mean pore size of microstructure, because it provides much more context to the machine learning model compared to porosity, it is denoted by the descriptor D^9 in Fig. 9(a) and falls into the *pore phase*. Finally, the fourth descriptor set quantifies the *orientation* of active material particles and their degree of alignment in a particular direction. From the results above we have seen that orientation plays a major role in shaping the ion percolation and electron conduction pathways. Here we have considered two anisotropy parameters a_1 and a_2, which form the descriptors D^{10} and D^{11} as shown in Fig. 9(a). The details of each descriptor calculation are discussed in the Methodology section above.

Step 3:

For each given electrode structure, its physical descriptors from D^1 to D^{11} (as shown in Fig. 9(a)), i.e. each descriptor is transformed into a diverse set of features. This descriptor featurization is done by transforming each of them into multiple features by applying the prototypical function. The functions referred to as F^1 to F^9 are X, $1/X$, $X^{0.5}$, $X^{-0.5}$, X^2, $1/X^2$, X^3, $1/X^3$, and $\ln(X)$ respectively as shown in Fig. 9(a), where descriptor (D) value replaces X in each function. The resulting feature vector has a dimension of 11×9. The final feature vector is generated by cross multiplying the above feature vector with itself. This multiplication generates linear and non-linear combinations of two descriptors as shown in Fig. 9(a), with a dimension of $11 \times 9 \times 50$.

Step 4: Since the input features (or simply features) can be correlated to each other resulting in redundancy and multicollinearity, so we perform Descriptor-Descriptor correlation analysis (c.f. Fig. 9(b)). The removal of redundant features from the data is important since it provides the ML algorithm with physically meaningful variation in the input-output set. This eliminates the noise in data and creates a computationally light regression model for effective properties prediction. We perform correlation analysis on the input set, involving the calculation of pair-wise feature-feature linear correlation coefficient heat map. When the feature has a high degree of correlation they have a high Pearson's correlation. In general, a balance of several features needs to be established, otherwise, it leads to issues of either overfitting or underfitting. So, in this work we used a threshold correlation coefficient of 0.9, implying features correlated beyond 0.9 are considered to be 1, while correlation below 0.9 is changed to 0, binarizing the correlation map. Furthermore, the highly correlated features are then eliminated, resulting in key features with unique information about the microstructure (refer to Supporting Information for further details). In step 4 we also trim down our dataset by removing outliers within the output dataset which contains extreme values of effective properties (c.f. Fig. 9(b)). This is done to avoid training the model on extremely unlikely values of the output and preventing skewing and convergence issues. The outlier removal criteria are set to remove the top and bottom 1 percentile of the output values (refer to Supporting Information for more details).

Step 5: Fig. 9(b) shows step 5, where the generated finalized dataset is then randomized and split into testing and training datasets in a ratio of 80:20 respectively. The current machine learning workflow is aimed towards developing a regression model based on the supervised machine learning methods for predicting effective properties.

Step 6: It involves the training, testing, and comparing the various supervised learning-based regression models including Linear regression, Lasso regression, ElasticNet, Ridge regression, Decision Tree, Adaboost, and Gradient Boost[71] (c.f. Fig. 9(b)). These supervised learning models fall into three categories: Linear (Linear, Lasso, Ridge, ElasticNet), Decision tree, and Ensemble (Adaboost, Gradient Boost) based models. Linear models are the simplest model where the target output is the linear combination of the input features. The benefit of such a model is the low computational cost for training, testing, and deployment along with the physically interpretable results. Each linear model considered here also has its distinct advantages as discussed later. The decision tree models are a non-parametric method, which learns decision making from the training data features and grows trees with branching decision nodes. The model uses several subfunctions applied to the subdomain of the data. Decision trees are interpretable and have low computational costs but can easily overfit data. Finally, the ensemble methods (AdaBoost, Gradient Boost) are powerful because they combine the base estimations from several methods increasing the overall robustness and accuracy of predictions. The mathematical details of these methods have been added to the Supporting Information. The ML models are tested using three metrics for accuracy evaluation including mean absolute error (MAE) (c.f. Eq. (9)), coefficient of determination (R^2) (c.f. Eq. (10)) and relative error prediction (c.f. Eq. (11)).

$$MAE = \frac{1}{N}\sum_{i=1}^{N}\left|y_i^{true} - y_i^{pred}\right| \tag{9}$$

$$R^2 = 1 - \frac{\sum_{i=1}^{N} (y_i^{true} - y_i^{pred})^2}{\sum_{i=1}^{N} (y_i^{mean} - y_i^{pred})^2} \tag{10}$$

$$\text{Relative error prediction} = \frac{\hat{y}_i^{true} - y_i^{pred}}{\hat{y}_i^{true}}, \; i = 1....N \tag{11}$$

Tortuosity:

Fig. 10(a) shows the coefficient of determination (R^2, also referred to as accuracy) of tortuosity prediction for various supervised learning models. All the linear models perform quite similarly to each other with linear regression having slightly higher accuracy compared to the ridge, lasso, and elastic net which have equal accuracy. The decision tree model is slightly better than the linear models, while the best performing model is gradient boost. Table 1 shows that the gradient boost model's testing accuracy is greater than 0.91 at predicting tortuosity in any of three directions while the training accuracy is greater than 0.95. Fig. 10(b) shows the predicted tortuosity vs true tortuosity values for the testing of the best-performing gradient boost model while Fig. 10(c) shows the relative error in predictions. The mean absolute error in predicting tortuosity is about ~0.24 for both training and testing scenarios from Table 1. The gradient boost model performs better because it is based on the generation of an ensemble of trees where it keeps adding trees to improve the accuracy of the model and reduce bias. This makes it more resilient to outliers and random artifacts in data. Since it is known that tortuosity has outliers i.e., reaches extremely high values at low porosities as seen in Fig. 3(b). In comparison to gradient boost, a single decision tree has a higher error, because it is more prone to overfitting data i.e. small artifacts within an overly complex tree network can lead to completely different predictions. Fig. 10(b) also shows that tortuosity in the X, Y, and Z directions have a similar span of values because of the randomized dataset for testing with the inclusion of all kinds of electrode structures, though most of the values are between 1-100. From the predicted and true values, we can infer the relative error using Eq. (11), with it being high for the lower tortuosity values due to division as shown in Fig. 10(c). Also, since here we minimize the absolute error during the model training relative error is higher, instead, we can choose relative error to be minimized. Overall we demonstrate the best model capable of predicting a wide range of tortuosity values, with the 5-95 percentile range of the tortuosity values lying between -40 to 50% error band, which is reasonably accurate considering our comprehensive dataset consists of various shapes, AM volume fraction, binder volume fraction, size and orientation of particles.

Electronic Conductivity:

Fig. 11(a) shows the coefficient of determination of electronic conductivity predictions comparing the various supervised learning models. All the supervised learning models perform similarly to each other with all of them having an accuracy above 0.95 and are indistinguishable from each other. This is because electronic conductivity is theoretically bounded to lie between zero and the material's intrinsic electronic conductivity unlike tortuosity likewise the normalized electronic conductivity values span a theoretical range of 0-1, with fewer outliers encountered. Here we find that the gradient boost model performs best with an accuracy of 0.99 in all three directions as observed in Table 2. It also has a mean absolute error in predicting electronic conductivity of less than ~0.03 in training and testing. Fig. 11(b) shows that normalized electronic conductivity lies between ~0.05 to ~0.7, with the predicted values matching the true values for virtually all the electrode structure ranges. Overall we demonstrate a best-supervised learning model capable of predicting a wide range of electronic conductivity values, from Fig. 11(c) with the 5-95 percentile range of the electronic conductivity values lying between the ± 6% error band, which is reasonably accurate considering our comprehensive dataset consists of various AM volume fraction, binder volume fraction, AM particle size and orientation.

Interfacial area:

Fig. 12(a) shows the coefficient of determination of various supervised learning models for predicting specific surface area (a_{01}, a_{12}, a_{02}). All the models are highly accurate with an accuracy of more than 0.95, out of which the gradient boost model performs consistently quite well here along with other effective properties. Table 3 shows that it has an accuracy of 0.99 for all the three specific surface area predictions, along with the mean absolute error of less than 0.121 across training and testing. Fig. 12(b) shows the plot for the true vs predicted value for testing the best-performing gradient boost model, with virtually all points lying on the y=x line. Fig. 12(c) shows the relative error in predictions for the same, with the 5-95 percentile range corresponding to a ± 7% error band. Fig. 12(c) also shows that the three interfacial area values span a different range of values, with a_{01}(pore-AM) showing the largest range from almost zero to ~400k, a_{02}(pore-binder) exhibiting an intermediate range from ~40k to ~200k, and a_{12}(AM-binder) having the smallest range from ~80k to ~200k. We observe that the pore-binder and AM-binder interfacial area have a minimum value because all the electrode structures contain an additional binder phase with a volume fraction between 5-10%, implying the binder will cover a certain portion of AM particles and form an interface with pore space. AM-pore interface, which is an electrochemically active interface, can have a very low value resulting from the coverage due to the binder phase, coupled with a larger particle of AM causing further reduction in area, on other hand, it also takes the highest value for smaller electrode particles with minimal binder coating.

Although we have achieved more than 90% accuracy across various properties, the performance of the machine learning model can be further increased via multiple paths, by increasing the training sample set i.e having a more extensive set of microstructure datasets through the incorporation of experimental and computational datasets. Secondly increasing the input features i.e. through exhaustive microstructural characterization and using feature selection to add *meaningful* features which explain the model and use the effective property as a selection criterion. We can also improve the robustness of the model by the randomized splitting of training via k-fold cross validation and ML model hyperparameter tuning to find an optimal model.

Feature Ranking:

We have based our ML model for effective property prediction on the use of a high dimensional feature vector as an input, which contains the physical characteristic information of the microstructure and thus creates a highly accurate model with an accuracy of more than 90%. This high-dimensional feature vector is created by feature generation and self cross-multiplication of features generating complex features with a linear and non-linear combination from the microstructural descriptors (c.f. Fig. 9(a)). This in turn has higher predictive power than simple physical descriptors and helps in developing an accurate ML model. The detailed investigation of physical descriptors has been performed in Figure 2, but it is practically impossible and irrelevant to investigate each feature of the high dimensional feature vector (4950 features), instead, we rely on the supervised learning model. When the supervised machine learning model is finished training, it assigns relative importance to each feature in predicting the output, which determines the feature ranking.

Here we have presented the feature ranking with the top 3 most important features contributing to tortuosity, conductivity, and interfacial area models. Fig. 13(a) shows that within the tortuosity model the contribution from the top 3 features is highly unequal, with the first feature contributing ~80%. The first feature is γ^3/φ^3 (i.e. overlap/mean pore size), which implies that with an increase in overlap or decrease of pore size the tortuosity will increase. This can be explained, by the fact that when we pack more active material, it leads to higher overlap and smaller pore size which in turn leads to constricted ionic percolation pathways, increasing tortuosity. The second and third features contribute about ~3-4%, and both of them show inverse proportionality to φ (i.e. mean pore size), which follows the reasoning mentioned above. Fig. 13(b) shows that in the electronic conductivity model the contribution from the top 3 features is even more disproportionate, with the first feature contributing ~90%. This feature is based on the $v_{AM}^2\,\gamma^{0.5}$ (i.e. vol. fraction of active material and overlap), which implies that when packing density is increased (increasing v_{AM}), it inturn increases overlap of particle creating extensive electron conduction pathways, resulting in increased electronic conductivity. The second and third features contribute to ~2-3%, which are dependent on the eccentricity of the particle, where an increase in eccentricity increases the connection between particles increasing the electronic conductivity. On another hand, the third feature has an inverse proportion to eccentricity, because it might have a negative weight associated with it. Fig. 13(c) shows the top feature for each interfacial area model (a_{01}, a_{02}, a_{12}), with a more equitable distribution of importance across features. The most critical feature for predicting a_{01} is $1/\psi R_{eq}$ (i.e. sphericity and equivalent radius), of this equivalent radius, is inversely proportional because specific surface area increases as the active material particle size decrease. We also know that a sphere is an object which minimizes surface area for the most volume and its sphericity is maximum with the value of one, while all other shapes have sphericity less than one. This implies further an active material shape deviates from spherical geometry, it will have smaller sphericity and correspondingly higher interfacial area proving the inverse proportion to sphericity. The a_{02} surface area quantifies the interfacial area between the secondary phase and pore phase with the most important feature being $v_S/R_{eq}^{0.5}$ (c.f. Fig. 13(c)), so as the secondary phase content increases (v_S) or the size of particle decreases, it effectively increases the interface between the secondary phase and pores. Finally, a_{12} is the interface between AM particle and secondary phase and as a result is highly correlated to $v_{AM}^3 v_S^3$, an increase in either active material content (v_{AM}) or secondary phase content (v_S) will increase the interface between the AM-secondary phase.

Conclusions:

In this study, we have developed a machine learning (ML) based predictive tool to estimate the effective properties of the electrode structure based on its physical descriptors. Building a comprehensive dataset of ~17000 stochastically generated porous electrode microstructure with the varied composition of active material (AM) and binder phase, ellipsoidal particle shapes, sizes, and orientation. The structure is characterized for its effective properties including tortuosity, electronic conductivity, and interfacial area with variability rooted in the microstructural features. We have demonstrated this for graphite as an exemplar system with descriptors quantifying the structural aspects, so the method is extensible to other porous systems with similar morphological characteristics.

The comprehensive ellipsoidal shapes have different morphologies including prolate, oblate, bladed, and spherical. Among the various particle shapes, the random alignment of spherical particles minimizes the tortuosity followed by prolate, bladed, and oblate particles ($\varepsilon \geq 0.3$), whereas electronic conductivity follows the opposite trend. There is a tradeoff between the electronic conductivity and tortuosity with AM packing, with a linear increase in electronic conductivity exponentially increasing tortuosity. This apparent tradeoff can be minimized by the alignment of non-spherical particle morphologies to improve the transport direction properties and maintain the specific surface area.

From the comprehensive effective property dataset, we determine that the empirical relations such as Bruggeman's law and for the specific surface area are valid for high porosity and limited morphology due to not considering the presence of multiphase, anisotropy, and overlapping of particles. The current machine learning workflow enables the solution to this key research question, i.e. describing the microstructural effective properties of the electrode in terms of its relevant physical descriptors of it. We recognize the strong dependence of effective property on the electrode microstructure morphology and propose physically meaningful descriptors to quantify composition, active material shape, orientation, and pore-phase. These physical descriptors are featurized and transformed through the application of various operator functions and cross multiplied with each other. A reduced descriptor dimension space is identified through minimizing descriptor-descriptor correlation. These featurized physical descriptors serve as the input to the supervised machine learning model with effective properties as the output. An accurate supervised machine learning model is built with accuracy greater than 90% across all the effective properties based on the gradient boost model. The physical descriptors improve the prediction accuracy of effective properties as compared to the empirical relations.

We also performed the feature ranking through the trained supervised machine learning model, which improves the explainability and understanding of the underlying relationship between the physical descriptors and the output of the model. The ranking analysis can also help in developing a simple yet accurate reduced dimensional representation of the output. Ultimately this analysis also paves the way to automate the process of empirical relation development truly from observations (i.e. data samples) through a trained supervised machine learning model.

Supporting Information

The mathematical details of the machine learning model and the microstructural characterization for effective property and physical descriptors are presented in the supporting information.

Acknowledgment

Financial support from the National Science Foundation under grant no. CMMI – 1901906 is gratefully acknowledged. PPM acknowledges NSF CMMI data science supplement funding from this grant.

Declaration of Interests

The authors declare no competing interests.

List of Figures

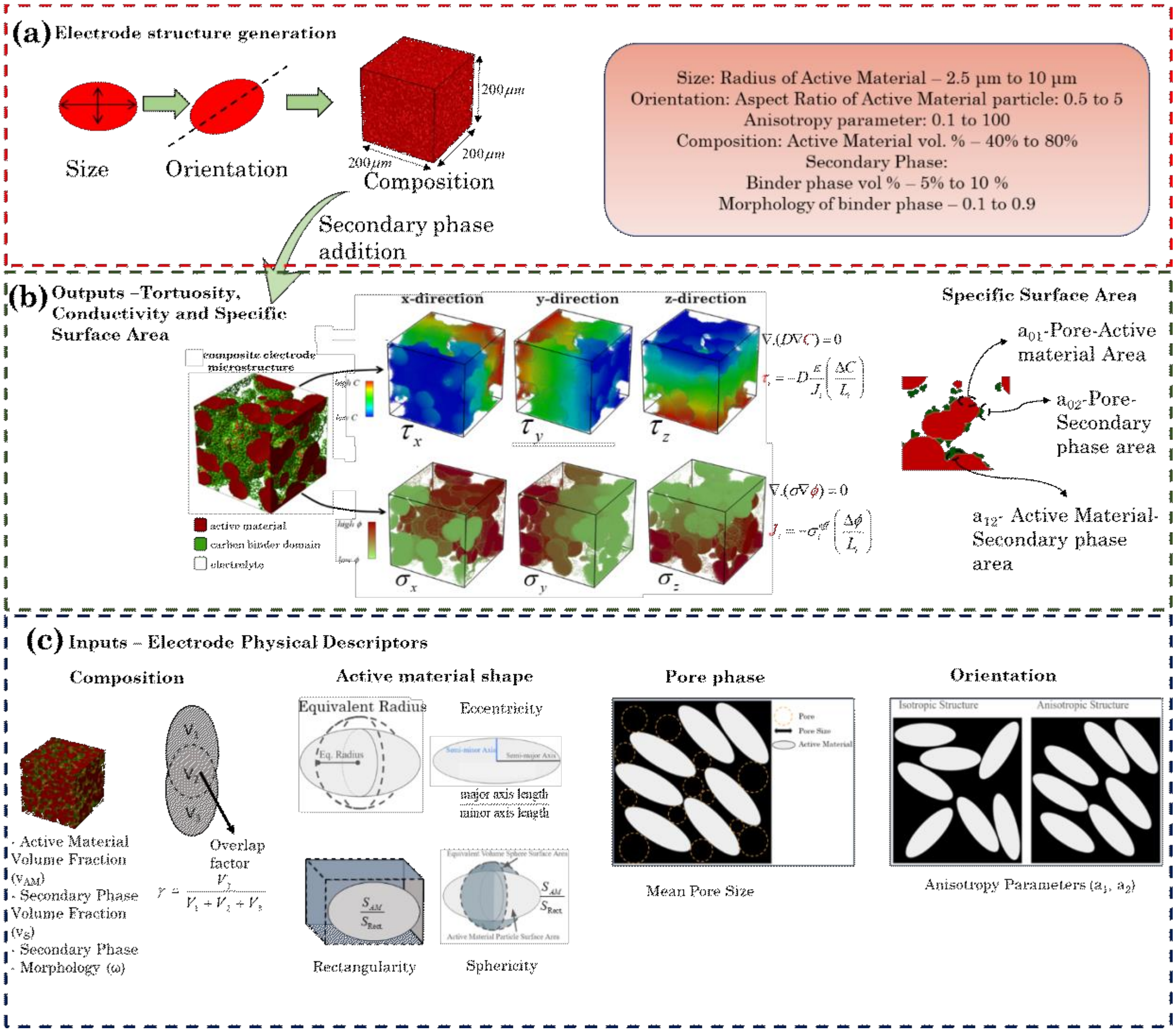

Figure. 1. Three-dimensional stochastic electrode structure generation (input) and effective properties (output): (a) The generated electrode microstructure's range of composition, ellipsoidal particle sizes, and orientation along with interfacial energy-based deposition of binder domain[13] (b) Characterization of these electrode microstructures for the effective properties i.e. tortuosity, electronic conductivity in the three directions and calculation of specific surface area for the three interfaces consisting of active material (AM) – secondary phase (binder), AM–pore and pore-secondary phase interface. (c) Characterizing electrodes via physical descriptors which have been categorized into four broad categories including Composition, Active material shape, Orientation, and Pore phase; Composition of electrode microstructure consists of active material volume fraction (v_{AM}), secondary phase volume fraction (v_S), secondary phase morphology (ω) and overlap factor; Active material shape features include quantification of shape factors such as equivalent radius, eccentricity, rectangularity, and sphericity for quantifying the active material

particle geometry; Pore phase quantification includes the mean pore size of the microstructure; Orientation of microstructure is quantified by using anisotropy parameters (a_1, a_2)

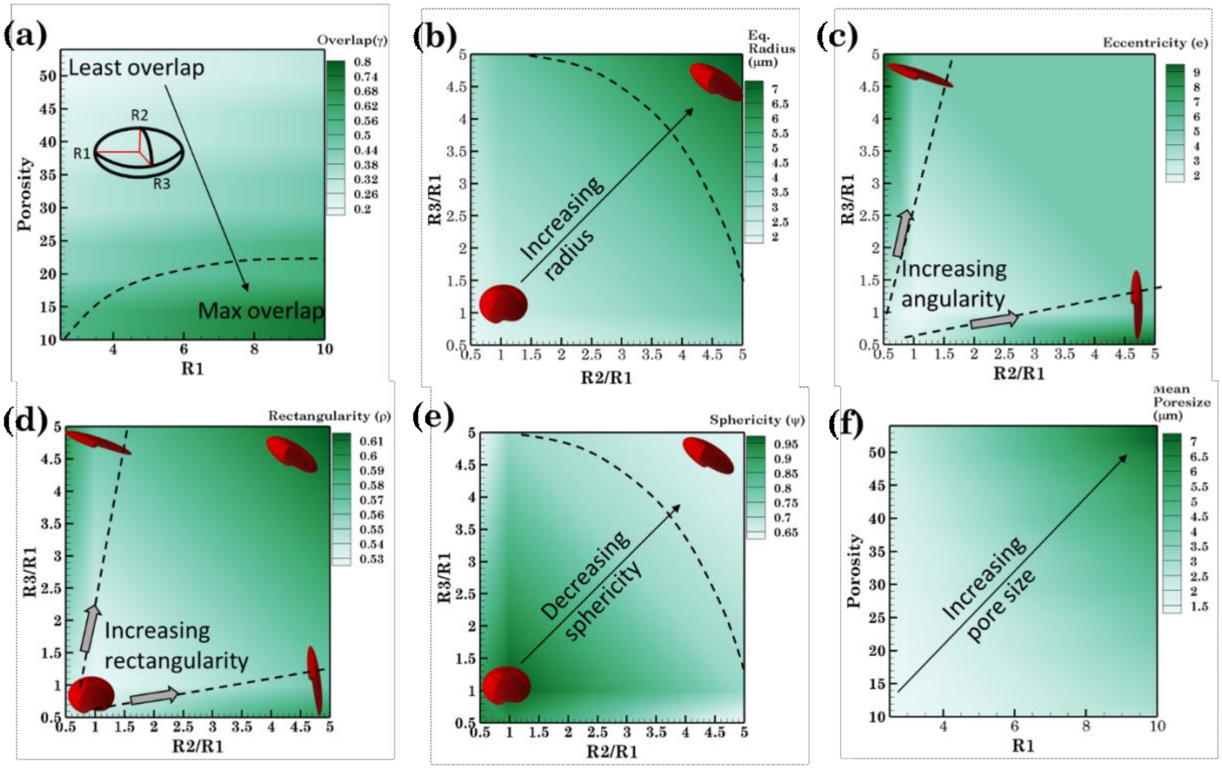

Figure 2. Electrode's physical descriptor (a) Varying overlap of ellipsoidal particles with different radius and packing fraction of active material (b) equivalent radius of the ellipsoidal particle with varying axis lengths (c) Eccentricity of ellipsoidal with varying axis lengths (d) Rectangularity of ellipsoidal particles with varying axis lengths (e) Sphericity of ellipsoidal particle with varying axis lengths (f) Mean pore size of microstructures with the differing radius of particles and packing fraction of active material

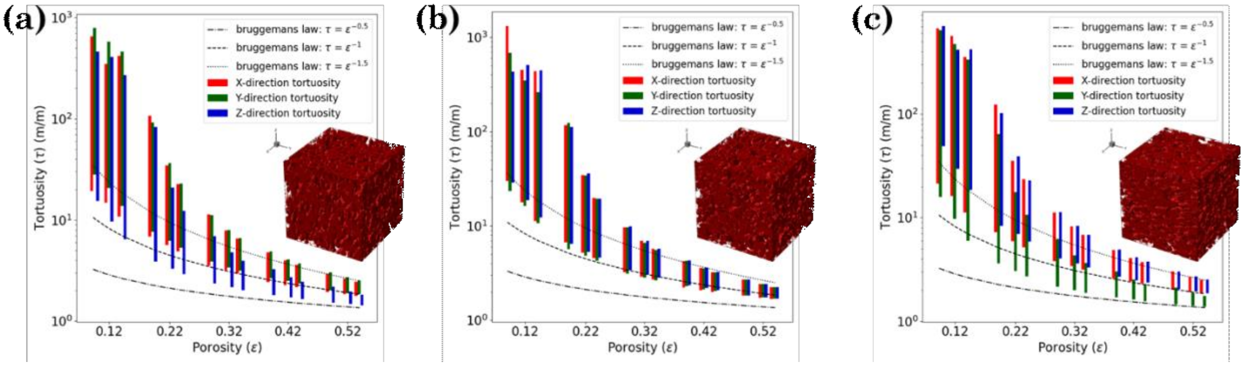

Figure 3. Effect of active material alignment on tortuosity: (a) Z-direction alignment causes tortuosity to be smaller in the Z direction which is apparent at higher porosities (b) random alignment leads to similar tortuosity in all directions, and (c) alignment perpendicular to Z-direction causes higher tortuosity in that direction which is apparent at higher porosities

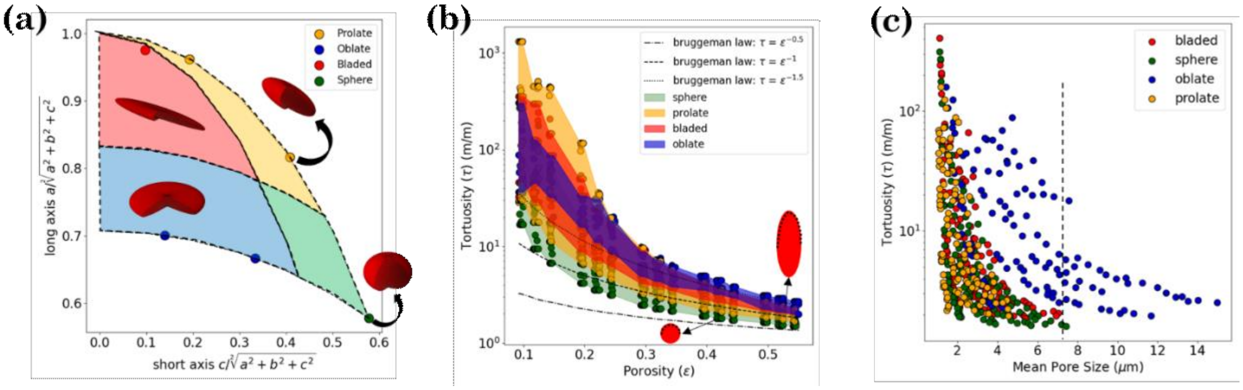

Figure 4. Effect of active material shape on tortuosity: (a) shape classification for ellipsoids based on the Zingg[66] diagram, (b) tortuosity with different active material ellipsoidal shapes, and (c) tortuosity vs. mean pore size for different active material ellipsoidal shapes.

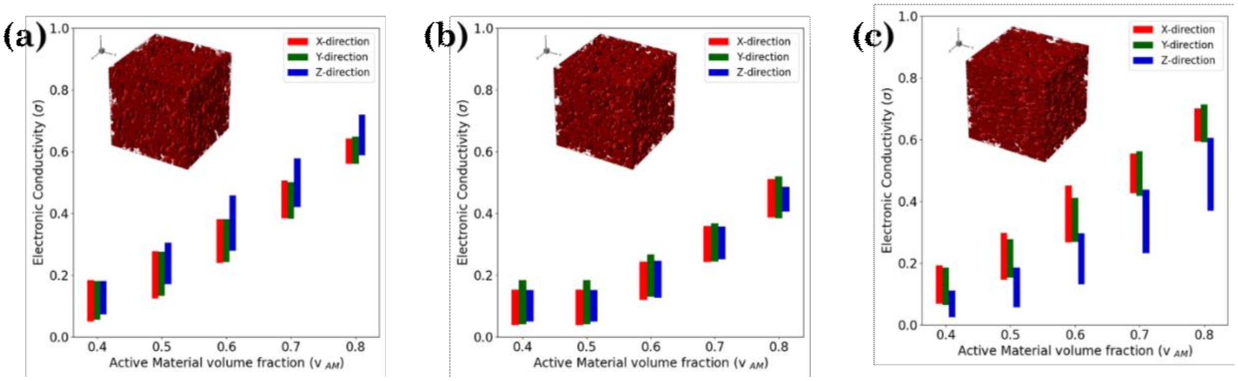

Figure 5. Effect of active material alignment on electronic conductivity: (a) Z-direction alignment causes the electronic conductivity to be higher in that direction at high volume fractions, (b) random alignment leads to similar electronic conductivity in all directions, and (c) alignment perpendicular to Z-direction causes smaller electronic conductivity in that direction.

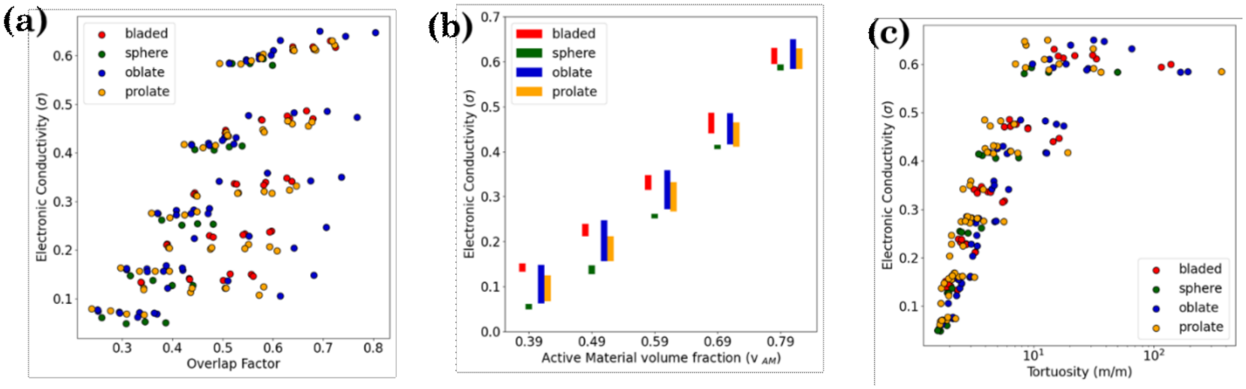

Figure 6. Effect of active material shape on electronic conductivity: (a) electronic conductivity variation with the overlap of particles, (b) electronic conductivity vs. active material volume fraction, and (c) electronic conductivity vs. tortuosity.

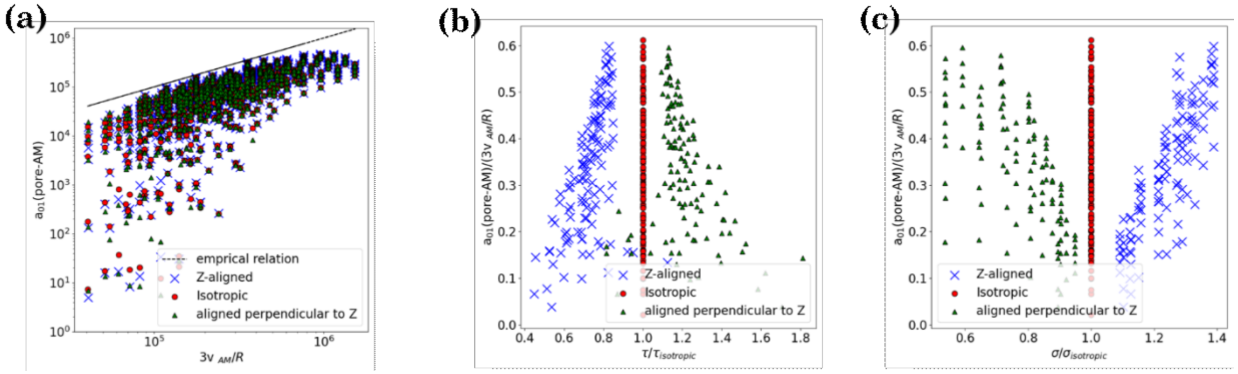

Figure 7. Effect of particle alignment on the specific surface area for different electrode microstructures (a) specific surface area comparison for microstructures with particles oriented along Z-direction, randomly oriented, and oriented perpendicular to Z-direction (b) Impact of particle alignment direction on the normalized tortuosity, normalized w.r.t. tortuosity of microstructure with randomly aligned particles (c) Impact of particle alignment direction on the normalized electronic conductivity, normalized w.r.t. conductivity of microstructure with randomly aligned particles

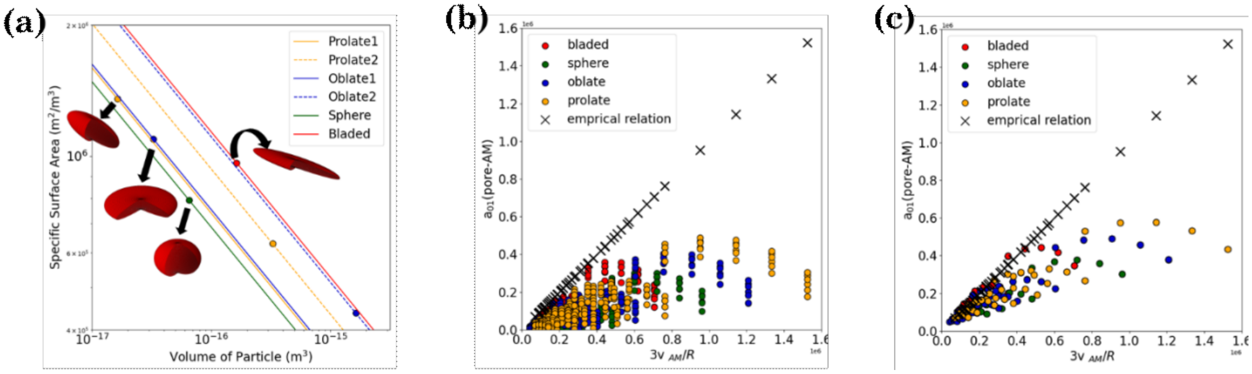

Figure 8. Microstructure consisting of differently shaped ellipsoid particles (a) specific surface area with a varying volume of the particle with different shapes (b) specific surface area of AM-pore interface comparison with idealized area based on the spherical non-overlapping electrode (c) specific surface area of (AM+binder)-pore interface

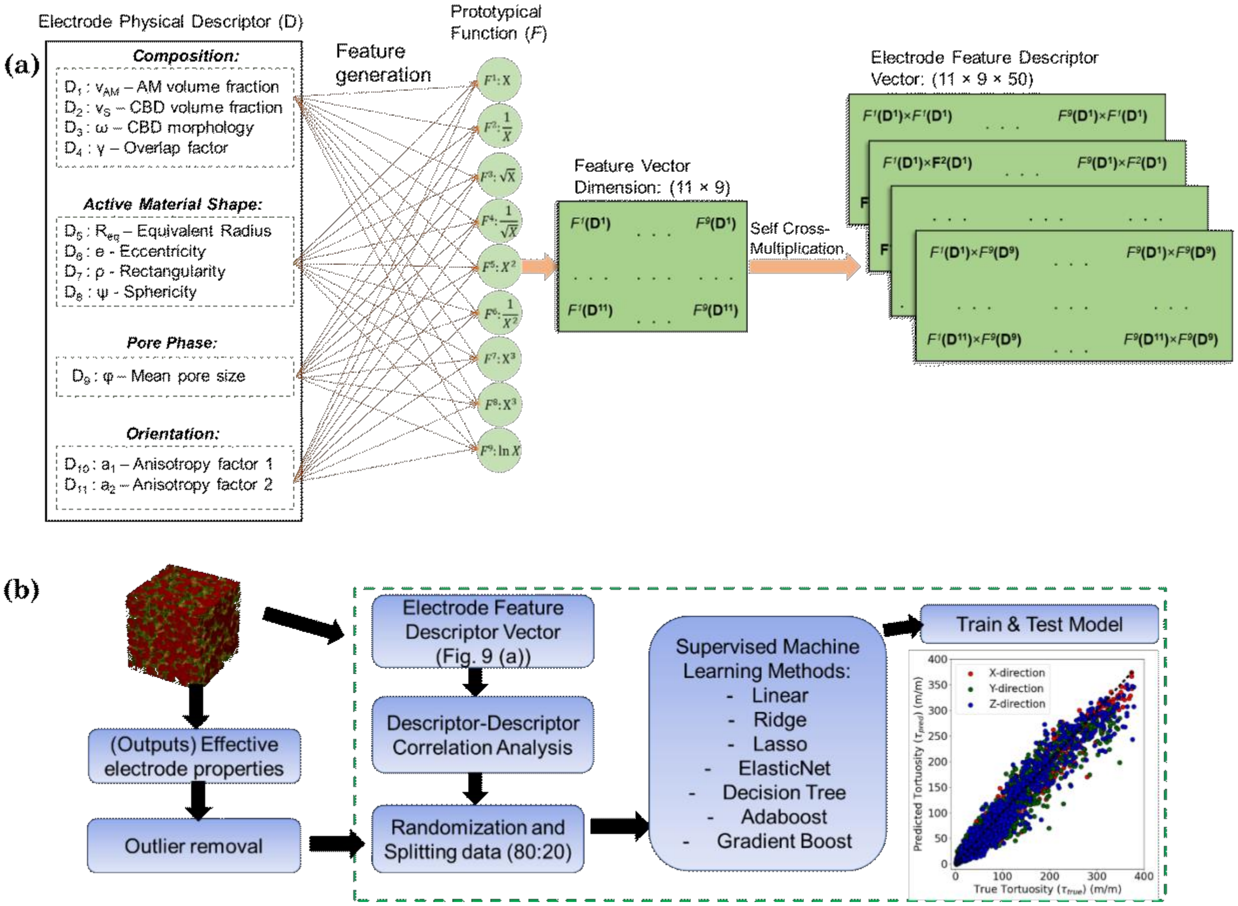

Figure 9. Machine Learning Framework (a) Creating electrode feature vector from a physical descriptor of microstructure through feature generation and cross-multiplication (b) Flowchart for machine learning algorithm for developing electrode microstructure – property relations

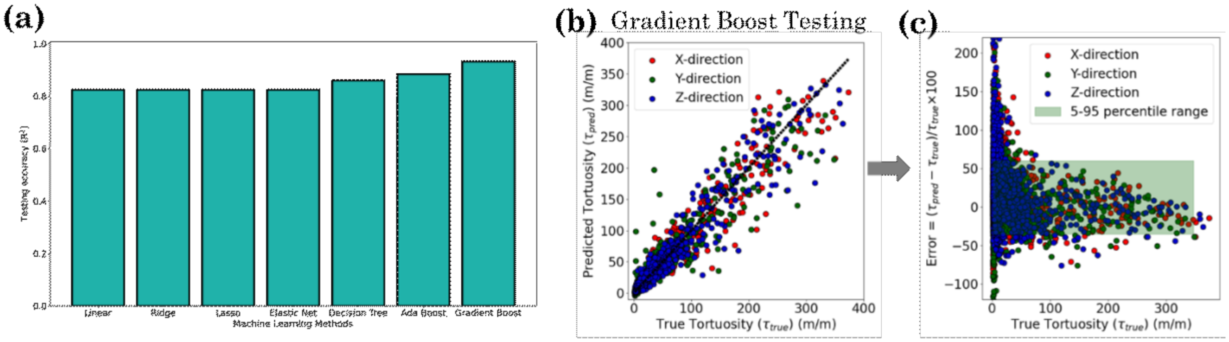

Figure 10. (a) Comparison of various supervised machine learning models for tortuosity (b) machine learning predicted results on the test set for comparison between true tortuosity value and predicted value (c) relative prediction error compared to true tortuosity

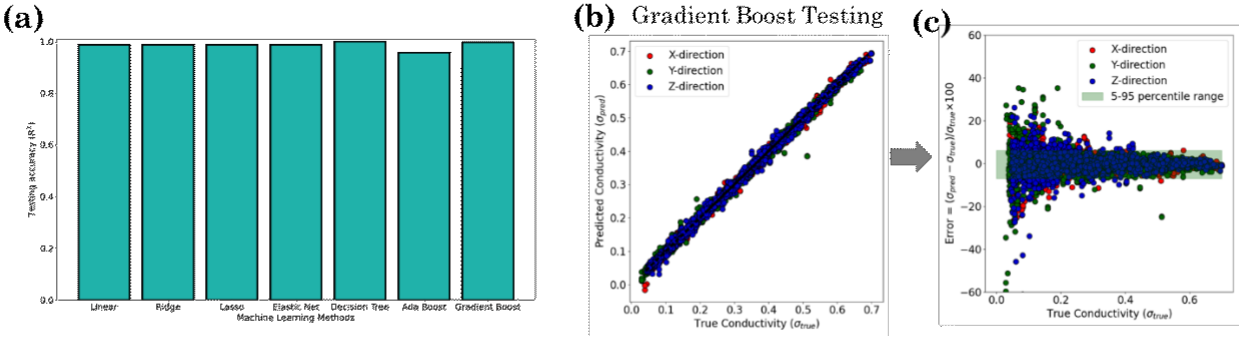

Figure 11. (a) Comparison of various supervised machine learning models for electronic conductivity (b) machine learning predicted results on the test set for comparison between true electronic conductivity and predicted value (c) relative prediction error compared to true electronic conductivity

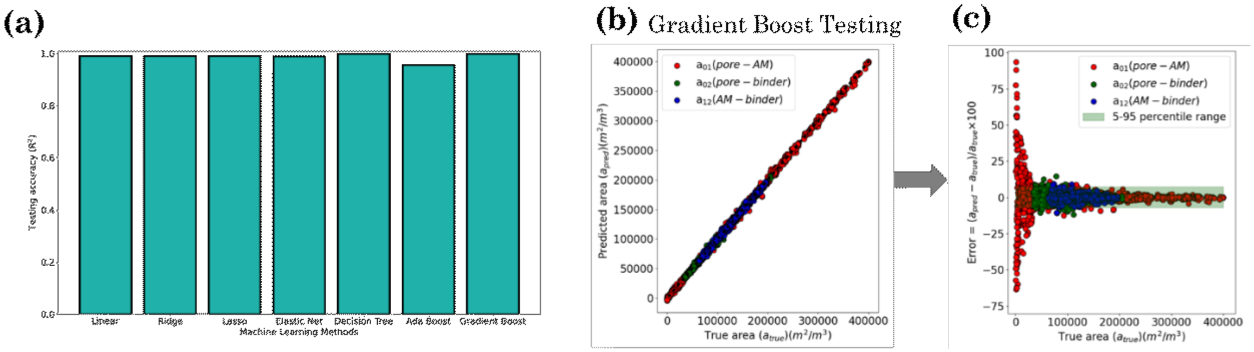

Figure 12. (a) Comparison of various supervised machine learning models for specific surface area (b) machine learning predicted results on the test set for comparison between true specific surface area and predicted value (c) relative prediction error compared to the true specific surface area

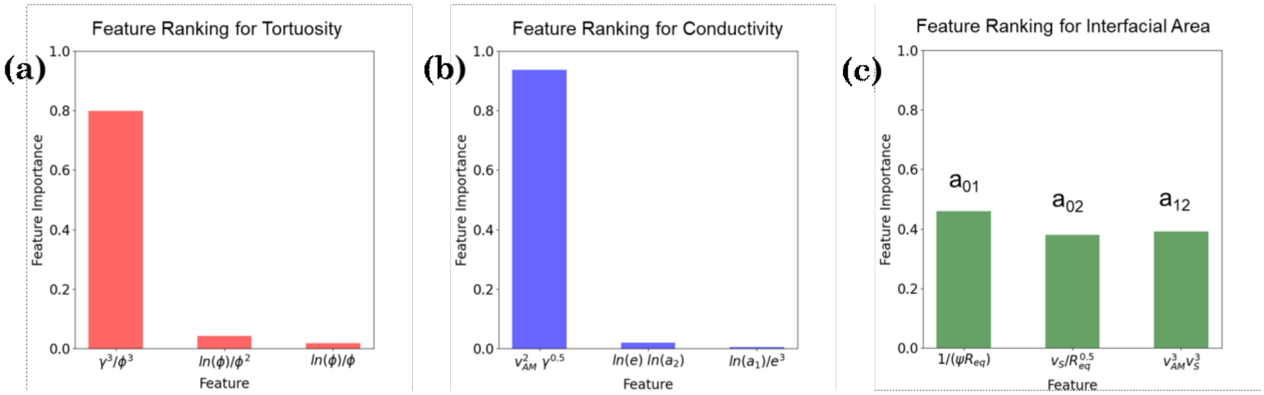

Figure 13. Feature ranking analysis showing the three most important features contributing to the ML model (a) Important features in the Tortuosity model (b) Important features in Electronic Conductivity model (c) Important features in the Interfacial area model

List of Tables:

	R^2			MAE		
	τ_x	τ_y	τ_z	τ_x	τ_y	τ_z
Train	0.97	0.97	0.96	0.203	0.202	0.216
Test	0.94	0.91	0.94	0.219	0.233	0.221

Table 1. The coefficient of determination (R^2) mean absolute error (MAE) for the tortuosity in three directions using the gradient boost model.

	R^2			MAE		
	σ_x	σ_y	σ_z	σ_x	σ_y	σ_z
Train	0.99	0.99	0.99	0.023	0.027	0.023
Test	0.99	0.99	0.99	0.027	0.030	0.025

Table 2. The coefficient of determination (R^2) mean absolute error (MAE) for the electronic conductivity in three directions using the gradient boost model.

	R^2			MAE		
	a_{01}	a_{02}	a_{12}	a_{01}	a_{02}	a_{12}
Train	0.99	0.99	0.99	0.093	0.012	0.007
Test	0.99	0.99	0.99	0.106	0.014	0.008

Table 3. The coefficient of determination (R^2) mean absolute error (MAE) for the specific surface area using the gradient boost model.

References:

(1) Fredericks, W. L.; Sripad, S.; Bower, G. C.; Viswanathan, V. Performance Metrics Required of Next-Generation Batteries to Electrify Vertical Takeoff and Landing (VTOL) Aircraft. *ACS Energy Letters* **2018**, *3* (12), 2989–2997. https://doi.org/10.1021/ACSENERGYLETT.8B02195.

(2) Yang, X. G.; Liu, T.; Ge, S.; Rountree, E.; Wang, C. Y. Challenges and Key Requirements of Batteries for Electric Vertical Takeoff and Landing Aircraft. *Joule* **2021**, *5* (7), 1644–1659. https://doi.org/10.1016/J.JOULE.2021.05.001.

(3) Wagner, F. T.; Lakshmanan, B.; Mathias, M. F. Electrochemistry and the Future of the Automobile. *Journal of Physical Chemistry Letters* **2010**, *1* (14), 2204–2219. https://doi.org/10.1021/JZ100553M.

(4) Thackeray, M. M.; Wolverton, C.; Isaacs, E. D. Electrical Energy Storage for Transportation—Approaching the Limits of, and Going beyond, Lithium-Ion Batteries. *Energy & Environmental Science* **2012**, *5* (7), 7854–7863. https://doi.org/10.1039/C2EE21892E.

(5) Nakayama, T.; Igarashi, Y.; Sodeyama, K.; Okada, M. Material Search for Li-Ion Battery Electrolytes through an Exhaustive Search with a Gaussian Process. *Chemical Physics Letters* **2019**, *731*, 136622. https://doi.org/10.1016/J.CPLETT.2019.136622.

(6) Kauwe, S. K.; David Rhone, T.; Sparks, T. D. Data-Driven Studies of Li-Ion-Battery Materials. https://doi.org/10.3390/cryst9010054.

(7) Huang, S.; Cole, J. M. A Database of Battery Materials Auto-Generated Using ChemDataExtractor. *Scientific Data 2020 7:1* **2020**, *7* (1), 1–13. https://doi.org/10.1038/s41597-020-00602-2.

(8) Kirklin, S.; Meredig, B.; Wolverton, C. High-Throughput Computational Screening of New Li-Ion Battery Anode Materials. *Advanced Energy Materials* **2013**, *3* (2), 252–262. https://doi.org/10.1002/AENM.201200593.

(9) Whittingham*, M. S. Lithium Batteries and Cathode Materials. *Chemical Reviews* **2004**, *104* (10), 4271–4301. https://doi.org/10.1021/CR020731C.

(10) Ellis, B. L.; Lee, K. T.; Nazar, L. F. Positive Electrode Materials for Li-Ion and Li-Batteries†. *Chemistry of Materials* **2010**, *22* (3), 691–714. https://doi.org/10.1021/CM902696J.

(11) Liu, Y.; Zhu, Y.; Cui, Y. Challenges and Opportunities towards Fast-Charging Battery Materials. *Nature Energy 2019 4:7* **2019**, *4* (7), 540–550. https://doi.org/10.1038/s41560-019-0405-3.

(12) Choi, J. W.; Aurbach, D. Promise and Reality of Post-Lithium-Ion Batteries with High Energy Densities. *Nature Reviews Materials 2016 1:4* **2016**, *1* (4), 1–16. https://doi.org/10.1038/natrevmats.2016.13.

(13) Mistry, A. N.; Smith, K.; Mukherjee, P. P. Secondary-Phase Stochastics in Lithium-Ion Battery Electrodes. **2018**. https://doi.org/10.1021/acsami.7b17771.

(14) Shearing, P. R.; Brandon, N. P.; Gelb, J.; Bradley, R.; Withers, P. J.; Marquis, A. J.; Cooper, S.; Harris, S. J. Multi Length Scale Microstructural Investigations of a Commercially Available Li-Ion Battery Electrode. *Journal of The Electrochemical Society* **2012**, *159* (7), A1023. https://doi.org/10.1149/2.053207JES.

(15) Komini Babu, S.; Mohamed, A. I.; Whitacre, J. F.; Litster, S. Multiple Imaging Mode X-Ray Computed Tomography for Distinguishing Active and Inactive Phases in Lithium-Ion Battery Cathodes. *Journal of Power Sources* **2015**, *283*, 314–319. https://doi.org/10.1016/J.JPOWSOUR.2015.02.086.

(16) Tariq, F.; Yufit, V.; Kishimoto, M.; Shearing, P. R.; Menkin, S.; Golodnitsky, D.; Gelb, J.; Peled, E.; Brandon, N. P. Three-Dimensional High Resolution X-Ray Imaging and Quantification of Lithium Ion Battery Mesocarbon Microbead Anodes. *Journal of Power Sources* **2014**, *248*, 1014–1020. https://doi.org/10.1016/J.JPOWSOUR.2013.08.147.

(17) Newman, J.; Thomas-Alyea, K. *Electrochemical Systems*; 2012.

(18) Newman, J. S.; Tobias, C. W. Theoretical Analysis of Current Distribution in Porous Electrodes. *Journal of The Electrochemical Society* **1962**, *109* (12), 1183. https://doi.org/10.1149/1.2425269/PDF.

(19) Doyle, M.; Fuller, T. F.; Newman, J. Modeling of Galvanostatic Charge and Discharge of the Lithium/Polymer/Insertion Cell. *Journal of The Electrochemical Society* **1993**, *140* (6), 1526–1533. https://doi.org/10.1149/1.2221597/PDF.

(20) Usseglio-Viretta, F. L. E.; Colclasure, A.; Mistry, A. N.; Claver, K. P. Y.; Pouraghajan, F.; Finegan, D. P.; Heenan, T. M. M.; Abraham, D.; Mukherjee, P. P.; Wheeler, D.; Shearing, P.; Cooper, S. J.; Smith, K. Resolving the Discrepancy in Tortuosity Factor Estimation for Li-Ion Battery Electrodes through Micro-Macro Modeling and Experiment. *Journal of The Electrochemical Society* **2018**, *165* (14), A3403. https://doi.org/10.1149/2.0731814JES.

(21) Ebner, M.; Chung, D.-W.; García, R. E.; Wood, V. Tortuosity Anisotropy in Lithium-Ion Battery Electrodes. *Advanced Energy Materials* **2014**, *4* (5), 1301278. https://doi.org/10.1002/AENM.201301278.

(22) Müller, S.; Eller, J.; Ebner, M.; Burns, C.; Dahn, J.; Wood, V. Quantifying Inhomogeneity of Lithium Ion Battery Electrodes and Its Influence on Electrochemical Performance. *Journal of The Electrochemical Society* **2018**, *165* (2), A339–A344. https://doi.org/10.1149/2.0311802jes.

(23) Rajendra, T.; Mistry, A. N.; Patel, P.; Ausderau, L. J.; Xiao, X.; Mukherjee, P. P.; Nelson, G. J. Quantifying Transport, Geometrical, and Morphological Parameters in Li-Ion Cathode Phases Using X-Ray Microtomography. *ACS Applied Materials & Interfaces* **2019**, *11* (22), 19933–19942. https://doi.org/10.1021/ACSAMI.8B22758.

(24) Mistry, A.; Usseglio-Viretta, F. L. E.; Colclasure, A. M.; Smith, K.; Mukherjee, P. P.; Fingerprinting Redox Heterogeneity in Electrodes during Extreme Fast Charging. *iopscience.iop.org* **2020**. https://doi.org/10.1149/1945-7111/ab8fd7.

(25) Fear, C.; Parmananda, M.; Kabra, V.; Carter, R.; Love, C. T.; Mukherjee, P. P. Mechanistic Underpinnings of Thermal Gradient Induced Inhomogeneity in Lithium Plating. *Energy Storage Materials* **2021**, *35*, 500–511. https://doi.org/10.1016/J.ENSM.2020.11.029.

(26) Vishnugopi, B. S.; Verma, A.; Mukherjee, P. P. Fast Charging of Lithium-Ion Batteries via Electrode Engineering. *Journal of The Electrochemical Society* **2020**, *167* (9), 090508. https://doi.org/10.1149/1945-7111/AB7FB9.

(27) Kabra, V.; Parmananda, M.; Fear, C.; Usseglio-Viretta, F. L. E.; Colclasure, A.; Smith, K.; Mukherjee, P. P. Mechanistic Analysis of Microstructural Attributes to Lithium Plating in Fast Charging. *ACS Appl. Mater. Interfaces* **2020**, *12*, 55795–55808. https://doi.org/10.1021/acsami.0c15144.

(28) Billaud, J.; Bouville, F.; Magrini, T.; Villevieille, C.; Studart, A. R. Magnetically Aligned Graphite Electrodes for High-Rate Performance Li-Ion Batteries. *Nature Energy 2016 1:8* **2016**, *1* (8), 1–6. https://doi.org/10.1038/nenergy.2016.97.

(29) Sander, J. S.; Erb, R. M.; Li, L.; Gurijala, A.; Chiang, Y.-M. High-Performance Battery Electrodes via Magnetic Templating. *Nature Energy 2016 1:8* **2016**, *1* (8), 1–7. https://doi.org/10.1038/nenergy.2016.99.

(30) Usseglio-Viretta, F. L. E.; Mai, W.; Colclasure, A. M.; Doeff, M.; Yi, E.; Smith, K. Enabling Fast Charging of Lithium-Ion Batteries through Secondary- /Dual- Pore Network: Part I - Analytical Diffusion Model. *Electrochimica Acta* **2020**, *342*, 136034. https://doi.org/10.1016/J.ELECTACTA.2020.136034.

(31) Mai, W.; Usseglio-Viretta, F. L. E.; Colclasure, A. M.; Smith, K. Enabling Fast Charging of Lithium-Ion Batteries through Secondary-/Dual- Pore Network: Part II - Numerical Model. *Electrochimica Acta* **2020**, *341*, 136013. https://doi.org/10.1016/J.ELECTACTA.2020.136013.

(32) Bae, C.; Erdonmez, C.; … J. H.-A.; 2013, undefined. Design of Battery Electrodes with Dual-scale Porosity to Minimize Tortuosity and Maximize Performance. *Wiley Online Library* **2013**, *25* (9), 1254–1258. https://doi.org/10.1002/adma.201204055.

(33) Nemani, V. P.; Harris, S. J.; Smith, K. C. Design of Bi-Tortuous, Anisotropic Graphite Anodes for Fast Ion-Transport in Li-Ion Batteries. *J Electrochem Soc* **2015**, *162* (8), A1415–A1423. https://doi.org/10.1149/2.0151508JES.

(34) Torquato, S.; Rev., H. H. J.-Appl. Mech.; 2002, undefined. Random Heterogeneous Materials: Microstructure and Macroscopic Properties. *asmedigitalcollection.asme.org*.

(35) Landesfeind, J.; Hattendorff, J.; Ehrl, A.; Wall, W. A.; Gasteiger, H. A. Tortuosity Determination of Battery Electrodes and Separators by Impedance Spectroscopy. *Journal of The Electrochemical Society* **2016**, *163* (7), A1373–A1387. https://doi.org/10.1149/2.1141607JES/PDF.

(36) Landesfeind, J.; Ebner, M.; Eldiven, A.; Wood, V.; Gasteiger, H. A. Tortuosity of Battery Electrodes: Validation of Impedance-Derived Values and Critical Comparison with 3D Tomography. *Journal of The Electrochemical Society* **2018**, *165* (3), A469–A476. https://doi.org/10.1149/2.0231803JES/PDF.

(37) Malifarge, S.; Delobel, B.; Delacourt, C. Determination of Tortuosity Using Impedance Spectra Analysis of Symmetric Cell. *Journal of The Electrochemical Society* **2017**, *164* (11), E3329. https://doi.org/10.1149/2.0331711JES.

(38) Markevich, E.; Levi, M. D.; Aurbach, D. Comparison between Potentiostatic and Galvanostatic Intermittent Titration Techniques for Determination of Chemical Diffusion Coefficients in Ion-Insertion Electrodes. *Journal of Electroanalytical Chemistry* **2005**, *580* (2), 231–237. https://doi.org/10.1016/J.JELECHEM.2005.03.030.

(39) Liu, G.; Zheng, H.; Kim, S.; Deng, Y.; Minor, A. M.; Song, X.; Battaglia, V. S. Effects of Various Conductive Additive and Polymeric Binder Contents on the Performance of a Lithium-Ion Composite Cathode. *Journal of The Electrochemical Society* **2008**, *155* (12), A887. https://doi.org/10.1149/1.2976031.

(40) Zheng, H.; Li, J.; Song, X.; Liu, G.; Battaglia, V. S. A Comprehensive Understanding of Electrode Thickness Effects on the Electrochemical Performances of Li-Ion Battery Cathodes. *Electrochimica Acta* **2012**, *71*, 258–265. https://doi.org/10.1016/J.ELECTACTA.2012.03.161.

(41) Weber, R.; Cheng, J.-H.; Louli, A. J.; Coon, M.; Hy, S.; Dahn, J. R. Surface Area of Lithium-Metal Electrodes Measured by Argon Adsorption. *Journal of The Electrochemical Society* **2019**, *166* (14), A3250–A3253. https://doi.org/10.1149/2.1181913jes.

(42) Kashkooli, A. G.; Farhad, S.; Lee, D. U.; Feng, K.; Litster, S.; Babu, S. K.; Zhu, L.; Chen, Z. Multiscale Modeling of Lithium-Ion Battery Electrodes Based on Nano-Scale X-Ray Computed Tomography. *Journal of Power Sources* **2016**, *307*, 496–509. https://doi.org/10.1016/J.JPOWSOUR.2015.12.134.

(43) Zielke, L.; Hutzenlaub, T.; Wheeler, D. R.; Chao, C.-W.; Manke, I.; Hilger, A.; Paust, N.; Zengerle, R.; Thiele, S. Three-Phase Multiscale Modeling of a LiCoO 2 Cathode: Combining the Advantages of FIB-SEM Imaging and X-Ray Tomography. **2014**. https://doi.org/10.1002/aenm.201401612.

(44) Gelb, J.; Finegan, D. P.; Brett, D. J. L.; Shearing, P. R. Multi-Scale 3D Investigations of a Commercial 18650 Li-Ion Battery with Correlative Electron- and X-Ray Microscopy. *Journal of Power Sources* **2017**, *357*, 77–86. https://doi.org/10.1016/J.JPOWSOUR.2017.04.102.

(45) Yu, Y.-S.; Farmand, M.; Kim, C.; Liu, Y.; Grey, C. P.; Strobridge, F. C.; Tyliszczak, T.; Celestre, R.; Denes, P.; Joseph, J.; Krishnan, H.; Maia, F. R. N. C.; Kilcoyne, A. L. D.; Marchesini, S.; Leite, T. P. C.; Warwick, T.; Padmore, H.; Cabana, J.; Shapiro, D. A. Three-Dimensional Localization of Nanoscale Battery Reactions Using Soft X-Ray Tomography. *Nature Communications 2018 9:1* **2018**, *9* (1), 1–7. https://doi.org/10.1038/s41467-018-03401-x.

(46) Trembacki, B. L.; Mistry, A. N.; Noble, D. R.; Ferraro, M. E.; Mukherjee, P. P.; Roberts, S. A. Editors' Choice—Mesoscale Analysis of Conductive Binder Domain Morphology in Lithium-Ion Battery Electrodes. *Journal of The Electrochemical Society* **2018**, *165* (13), E725–E736. https://doi.org/10.1149/2.0981813JES/PDF.

(47) Choudhary, R.; on, H. G.-2017 I. C.; Comprehensive Review on Supervised Machine Learning Algorithms. *ieeexplore.ieee.org*. **(2017)**

(48) Kotsiantis, S. B. Supervised Machine Learning: A Review of Classification Techniques. *Informatica* **2007**, *31*, 249–268.

(49) Zhang, Y.; Tang, Q.; Zhang, Y.; Wang, J.; Stimming, U.; Lee, A. A. Identifying Degradation Patterns of Lithium Ion Batteries from Impedance Spectroscopy Using Machine Learning. *Nature Communications 2020 11:1* **2020**, *11* (1), 1–6. https://doi.org/10.1038/s41467-020-15235-7.

(50) Babaeiyazdi, I.; Rezaei-Zare, A.; Shokrzadeh, S. State of Charge Prediction of EV Li-Ion Batteries Using EIS: A Machine Learning Approach. *Energy* **2021**, *223*, 120116. https://doi.org/10.1016/J.ENERGY.2021.120116.

(51) Li, B.; Jones, C.; of, V. T.-J.; 2021, undefined. Overdischarge Detection and Prevention With Temperature Monitoring of Li-Ion Batteries and Linear Regression-Based Machine Learning. *asmedigitalcollection.asme.org*.

(52) Yamanaka, T.; … Y. T.-J. of T.; 2020, undefined. A Framework for Optimal Safety Li-Ion Batteries Design Using Physics-Based Models and Machine Learning Approaches. *iopscience.iop.org* **2020**. https://doi.org/10.1149/1945-7111/ab975c.

(53) Chen, Z.; Shi, N.; Ji, Y.; Niu, M.; Wang, Y. Lithium-Ion Batteries Remaining Useful Life Prediction Based on BLS-RVM. *Energy* **2021**, *234*, 121269. https://doi.org/10.1016/J.ENERGY.2021.121269.

(54) Fermín-Cueto, P.; McTurk, E.; Al, M. A.-E. and; 2020, undefined. Identification and Machine Learning Prediction of Knee-Point and Knee-Onset in Capacity Degradation Curves of Lithium-Ion Cells. *Elsevier*.

(55) Patil, M. A.; Tagade, P.; Hariharan, K. S.; Kolake, S. M.; Song, T.; Yeo, T.; Doo, S. A Novel Multistage Support Vector Machine Based Approach for Li Ion Battery Remaining Useful Life Estimation. *Applied Energy* **2015**, *159*, 285–297. https://doi.org/10.1016/J.APENERGY.2015.08.119.

(56) Berecibar, M. Machine-Learning Techniques Used to Accurately Predict Battery Life. **2019**.

(57) Severson, K. A.; Attia, P. M.; Jin, N.; Perkins, N.; Jiang, B.; Yang, Z.; Chen, M. H.; Aykol, M.; Herring, P. K.; Fraggedakis, D.; Bazant, M. Z.; Harris, S. J.; Chueh, W. C.; Braatz, R. D. Data-Driven Prediction of Battery Cycle Life before Capacity Degradation. *Nature Energy 2019 4:5* **2019**, *4* (5), 383–391. https://doi.org/10.1038/s41560-019-0356-8.

(58) Graczyk, K.; Reports, M. M.-S.; 2020, undefined. Predicting Porosity, Permeability, and Tortuosity of Porous Media from Images by Deep Learning. *nature.com*.

(59) Jung, J.; Yoon, J.; Park, H.; Kim, J.; Materials, H. K.-C.; 2019, undefined. An Efficient Machine Learning Approach to Establish Structure-Property Linkages. *Elsevier*.

(60) Vasilyeva, M.; Tyrylgin, A. Machine Learning for Accelerating Effective Property Prediction for Poroelasticity Problem in Stochastic Media. **2018**.

(61) Xu, H.; Zhu, J.; Finegan, D. P.; Zhao, H.; Lu, X.; Li, W.; Hoffman, N.; Bertei, A.; Shearing, P.; Bazant, M. Z. Guiding the Design of Heterogeneous Electrode Microstructures for Li-Ion Batteries:

Microscopic Imaging, Predictive Modeling, and Machine Learning. *Advanced Energy Materials* **2021**. https://doi.org/10.1002/AENM.202003908.

(62) *GeoDict The Digital Material Laboratory - Fraunhofer ITWM*. https://www.itwm.fraunhofer.de/en/departments/sms/products-services/geodict-digital-material-laboratory.html (accessed 2021-09-17).

(63) Mundszinger, M.; Farsi, S.; Rapp, M.; Golla-Schindler, U.; Kaiser, U.; Wachtler, M. Morphology and Texture of Spheroidized Natural and Synthetic Graphites. *Carbon N Y* **2017**, *111*, 764–773. https://doi.org/10.1016/J.CARBON.2016.10.060.

(64) Münch, B.; Holzer, L. Contradicting Geometrical Concepts in Pore Size Analysis Attained with Electron Microscopy and Mercury Intrusion. *Journal of the American Ceramic Society* **2008**, *91* (12), 4059–4067. https://doi.org/10.1111/J.1551-2916.2008.02736.X.

(65) Schindelin, J.; Arganda-Carreras, I.; Frise, E.; Kaynig, V.; Longair, M.; Pietzsch, T.; Preibisch, S.; Rueden, C.; Saalfeld, S.; Schmid, B.; Tinevez, J. Y.; White, D. J.; Hartenstein, V.; Eliceiri, K.; Tomancak, P.; Cardona, A. Fiji: An Open-Source Platform for Biological-Image Analysis. *Nature Methods*. Nat Methods July 2012, pp 676–682. https://doi.org/10.1038/nmeth.2019.

(66) *Beitrag zur Schotteranalyse - Research Collection*. https://www.research-collection.ethz.ch/handle/20.500.11850/135183 (accessed 2021-09-17).

(67) Bruggeman, D. A. G. Berechnung Verschiedener Physikalischer Konstanten von Heterogenen Substanzen. I. Dielektrizitätskonstanten Und Leitfähigkeiten Der Mischkörper Aus Isotropen Substanzen. *Ann Phys* **1935**, *416* (7), 636–664. https://doi.org/10.1002/ANDP.19354160705.

(68) Vijayaraghavan, B.; Ely, D. R.; Chiang, Y.-M.; García-García, R.; García, R. E. An Analytical Method to Determine Tortuosity in Rechargeable Battery Electrodes. *Journal of The Electrochemical Society* **2012**, *159* (5), A548. https://doi.org/10.1149/2.JES113224.

(69) Chung, D.; Ebner, M.; Ely, D.; … V. W.-… and S. in; 2013, undefined. Validity of the Bruggeman Relation for Porous Electrodes. *iopscience.iop.org* **2013**. https://doi.org/10.1088/0965-0393/21/7/074009.

(70) Xu, H.; Liu, R.; Choudhary, A.; Chen, W. A Machine Learning-Based Design Representation Method for Designing Heterogeneous Microstructures. *Journal of Mechanical Design, Transactions of the ASME* **2015**, *137* (5). https://doi.org/10.1115/1.4029768/383805.

(71) *1. Supervised learning — scikit-learn 0.24.2 documentation*. https://scikit-learn.org/stable/supervised_learning.html (accessed 2021-09-17).

Table of Contents Graphic: